

Unclassified

AD-A229 163

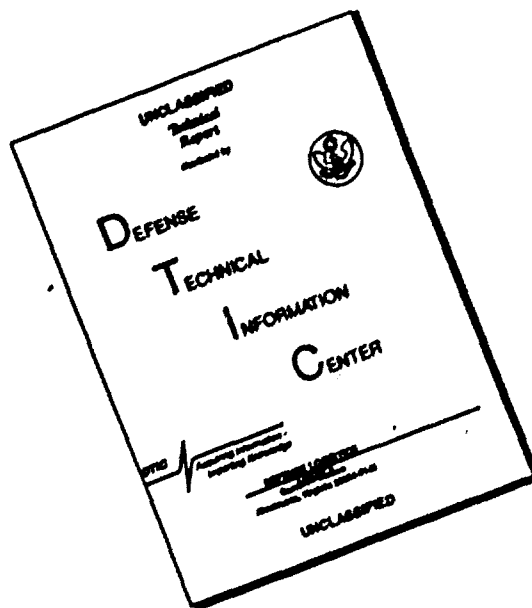
DOCUMENTATION PAGE

DTIC FILE COPY

Form Approved  
OMB No. 0704-0188

1a REPORT SECURITY CLASSIFICATION Unclassified			1b RESTRICTIVE MARKINGS		
2a SECURITY CLASSIFICATION AUTHORITY NOV 16 1990			3 DISTRIBUTION AVAILABILITY OF REPORT Approved for public release; distribution is unlimited		
2b DECLASSIFICATION/DOWNGRADING SCHEDULE			5 MONITORING ORGANIZATION REPORT NUMBER(S) AFOSR-TR- 90 1137		
4 PERFORMING ORGANIZATION REPORT NUMBER			7a NAME OF MONITORING ORGANIZATION AFOSR/NA		
6a NAME OF PERFORMING ORGANIZATION Massachusetts Institute of Technology			7b ADDRESS (City, State, and ZIP Code) Building 410, Bolling AFB DC 20332-6448		
6b OFFICE SYMBOL (if applicable)			9 PROCUREMENT INSTRUMENT IDENTIFICATION NUMBER AFOSR-89-U345		
8a NAME OF FUNDING/SPONSORING ORGANIZATION AFOSR/NA			10 SOURCE OF FUNDING NUMBERS		
8b OFFICE SYMBOL (if applicable) NA			PROGRAM ELEMENT NO 61102F	PROJECT NO 2306	TASK NO A1
9c ADDRESS (City, State, and ZIP Code) Building 410, Bolling AFB DC 20332-6448			10 WORK UNIT ACCESSION NO.		
11 TITLE (Include Security Classification) (U) "PROPULSION RESEARCH ON THE HYBRID PLUME ROCKET"					
12 PERSONAL AUTHOR(S) DRS F. R. Chung-Diaz, & T F. Yang					
13a TYPE OF REPORT ANNUAL	13b TIME COVERED FROM 9/1/89 TO 1/31/90	14 DATE OF REPORT (Year, Month, Day) 9/20/90	15 PAGE COUNT 26		
16 SUPPLEMENTARY NOTATION					
17 COSATI CODES			18 SUBJECT TERMS (Continue on reverse if necessary and identify by block number)		
FIELD	GROUP	SUB-GROUP			
19 ABSTRACT (Continue on reverse if necessary and identify by block number)					
<p>The propagation of rf waves launched in the end cell and central cell of the tandem mirror propulsion device has been investigated both theoretically and experimentally. Theoretically, a computer code has been developed to study the wave propagation in a nonhomogeneous magnetic field. It was found that the amplitude of the wave excited in the plasma peaked while approaching the resonance, but then damped out, indicating strong absorption of the wave by the plasma. The absorption took place near the axis and midplane of the device. The experimental results confirmed the theoretical prediction of the phenomena of the resonance effect. This means that the rf power is heating the plasma in center contrary to the earlier prediction that the heating was near the edge. Therefore higher heating efficiency can be possible. A very important discovery of this experiment was the broadening of the ICRF Fourier spectrum in the presence of the plasma. (Ref) ( )</p>					
20 DISTRIBUTION/AVAILABILITY OF ABSTRACT <input checked="" type="checkbox"/> UNCLASSIFIED/UNLIMITED <input checked="" type="checkbox"/> SAME AS RPT. <input type="checkbox"/> DTIC USERS			21. ABSTRACT SECURITY CLASSIFICATION Unclassified		
22a. NAME OF RESPONSIBLE INDIVIDUAL Dr Mitat Birkan			22b. TELEPHONE (Include Area Code) (202) 767-4938	22c. OFFICE SYMBOL AFOSR/NA	

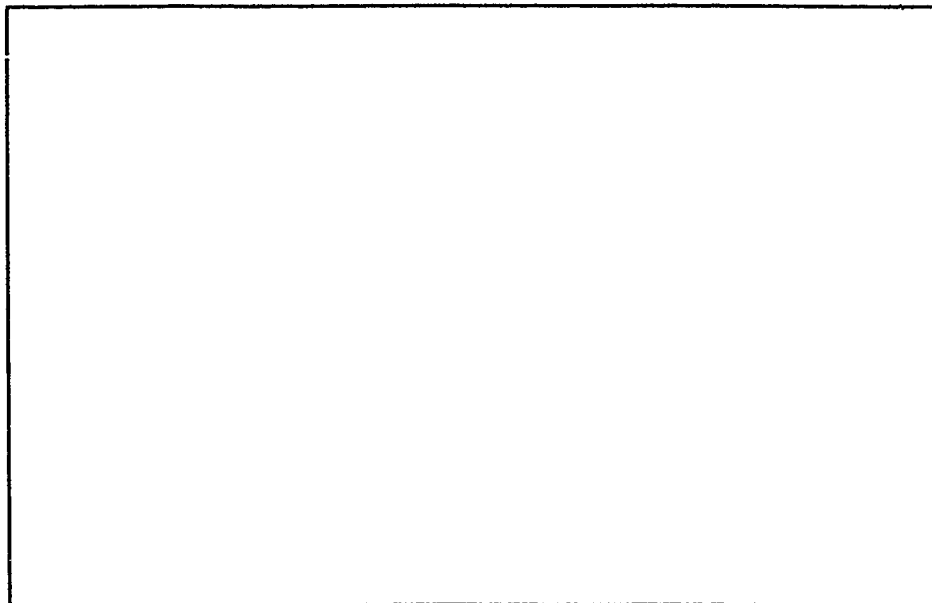
# DISCLAIMER NOTICE



**THIS DOCUMENT IS BEST  
QUALITY AVAILABLE. THE COPY  
FURNISHED TO DTIC CONTAINED  
A SIGNIFICANT NUMBER OF  
PAGES WHICH DO NOT  
REPRODUCE LEGIBLY.**

# MASSACHUSETTS INSTITUTE OF TECHNOLOGY

## P L A S M A F U S I O N C E N T E R



CAMBRIDGE, MASSACHUSETTS 02139

ASSOCIATED WITH  
DEPARTMENT OF ELECTRICAL ENGINEERING  
AND COMPUTER SCIENCE  
DEPARTMENT OF MATERIALS SCIENCE  
AND ENGINEERING  
DEPARTMENT OF MECHANICAL ENGINEERING  
DEPARTMENT OF NUCLEAR ENGINEERING  
DEPARTMENT OF PHYSICS  
FRANCIS BITTER NATIONAL MAGNET LABORATORY  
RESEARCH LABORATORY OF ELECTRONICS

90 11 15 073

**Final Technical Report on Propulsion Research  
on the Hybrid Plume Rocket  
for the period  
September 1, 1989 - January 31, 1990**

**F. R. Chang-Diaz\*  
T. F. Yang  
MIT Plasma Fusion Center**

**AFOSR Contract ~~#84-0198~~**

**89-0345**

**\*Astronaut Office of the Johnson Space Center**

# Contents

1	Introduction	2
2	Progress In Theoretical program	3
2.1	Analytical solution . . . . .	3
2.2	Computational Analysis . . . . .	5
2.3	Computational Results . . . . .	7
2.3.1	Collisionless . . . . .	7
2.3.2	Collisional . . . . .	11
3	Progress In Experimental Program	14
3.1	Diagnostics . . . . .	14
3.1.1	Langmuir Probe . . . . .	15
3.1.2	Interferometer . . . . .	16
3.1.3	Frequency Sweeping Operation . . . . .	16
3.1.4	Spectrometer . . . . .	17
3.1.5	$H_\alpha$ Array . . . . .	18
3.1.6	Diamagnetic Loop . . . . .	18
3.1.7	B-Dot Probe . . . . .	19
3.2	ICRH Wave Experimental . . . . .	19
3.2.1	experiment set-up . . . . .	19
3.2.2	experimental results . . . . .	19
3.2.3	Plasma Broadening of ICRF Spectrum . . . . .	21
3.2.4	Instability . . . . .	21



Accession For	
NTIS GRA&I	<input checked="" type="checkbox"/>
DTIC TAB	<input type="checkbox"/>
Unannounced	<input type="checkbox"/>
Justification	
By	
Distribution/	
Availability Codes	
Dist	Avail and/or Special
A-1	

## ABSTRACT

The propagation of rf waves launched in the end cell and central cell of the tandem mirror propulsion device has been investigated both theoretically and experimentally. Theoretically, a computer code has been developed to study the wave propagation in a nonhomogeneous magnetic field. It was found that the amplitude of the wave excited in the plasma peaked while approaching the resonance, but then damped out, indicating strong absorption of the wave by the plasma. The absorption took place near the axis and midplane of the device. The experimental results confirmed the theoretical prediction of the phenomena of the resonance effect. This means that the rf power is heating the plasma in center contrary to the earlier prediction that the heating was near the edge. Therefore higher heating efficiency can be possible. A very important discovery of this experiment was the broadening of the ICRF Fourier spectrum in the presence of the plasma. This broadening can be viewed as the detuning of the  $Q$  value of the resonance circuit due to plasma loading. Instability has been observed during the initial phase of the discharge followed by quiescent phase. Therefore the instability was stabilized. Large amount of data has been taken and is in the process of being analyzed. The analysis of plasma-gas interaction with coaxial injection of plasma and neutral gas has been completed which will be reported in detail separately. A collaboration effort with AVCO Research Laboratory has been established to examine the feasibility and method of using the high temperature plasma of this device for reentrance study for national space plane developmental effort.

## 1 Introduction

A tandem mirror plasma experimental facility was established for space propulsion developmental studies [1],[2],[3],[4],[5]. The experimental program encompasses three areas of study. First, to establish the fundamental plasma properties for the range of propulsion application. Second, to seek ways to maximize plasma heating, thus the improvement of power conversion efficiency and third, to study the plasma properties at the exhaust. The power conversion method will be to inject the rf power into the plasma to heat the ion species at the ion cyclotron resonance frequency (ICRF). Hence, understanding the physics of wave propagation in this device is fundamental to achieving the areas just mentioned. Wave propagation in a hot plasma contained in highly nonhomogeneous magnetic field is a very complicated problem which was briefly touched upon during the closing of the mirror fusion program. Nevertheless, in the theoretical area, extensive analytical work was done during early years of this program leading to the development of a computer code, BEACH. The achievements in theory and experiment are discussed in sections 2, 3, 4 and 5. The industrial participation

and the proposed scope of work are discussed in sections 5 and 8.

## 2 Progress In Theoretical program

### 2.1 Analytical solution

The wave propagation in a cylindrical geometry for cold plasma in nonhomogeneous magnetic field has been solved analytically and numerically. The mathematics involved is long and complex. Therefore the details will be discussed in a separate report ref[6]. Here, the greatly reduced but yet comprehensible theory is presented.

It can be shown that in the vacuum the Maxwell's equations can be reduced to the following differential equation:

$$\frac{d^2}{dr^2} E_z + \frac{1}{r} \frac{d}{dr} E_z - \left( \nu^2 + \frac{n^2}{r^2} \right) E_z = 0 \quad (1)$$

$$\frac{d^2}{dr^2} H_z + \frac{1}{r} \frac{d}{dr} H_z - \left( \nu^2 + \frac{n^2}{r^2} \right) H_z = 0 \quad (2)$$

The solutions to the above differential equations are the Bessel functions  $J_n(\nu r)$  and  $K_n(\nu r)$ .

It is seen that Maxwell's equations can be separated into two component solutions in a vacuum: TE and TM. While the presence of a plasma prevents a complete separation into the two modes, the Maxwell's equations can be simplified into two similar modes: the "nearly" TE mode,

$$\frac{d^2}{dr^2} H_{z1} + \frac{1}{r} \frac{d}{dr} H_{z1} + \left( k_{r1}^2 - \frac{n^2}{r^2} \right) H_{z1} = 0 \quad (3)$$

$$E_{z1} = z_1 H_{z1} \quad (4)$$

$$z_1 = \frac{\omega \mu_0 k_z B}{P(k_z^2 - k_z^2 S) + k_z^2 S} \quad (5)$$

and the electric modes(nearly TM),

$$\frac{d^2}{dr^2} E_{z2} + \frac{1}{r} \frac{d}{dr} E_{z2} + \left( k_{r2}^2 - \frac{n^2}{r^2} \right) E_{z2} = 0 \quad (6)$$

$$H_{z2} = y_2 E_{z2} \quad (7)$$

$$y_2 = \frac{i\omega\epsilon_0 k_z D D}{S(k_z^2 - k_0^2) R L k_0^2} \quad (8)$$

The plasma field solutions are then simply a sum of the nearly TE and nearly TM modes.

$$H_z = H_{z1} + y_2 E_{z2} \quad (9)$$

$$E_z = z_1 H_{z1} + E_{z2} \quad (10)$$

Where the solution of Equations 3 and 6 is the Bessel function  $J_n$

$$H_{z1} = H_p J_n(k_{r1} r) \quad (11)$$

$$E_{z2} = E_p J_n(k_{r2} r) \quad (12)$$

Given the boundary conditions and the transverse fields, the solution can be found to the power absorption problem. However, the form of the solution is extremely complex and any physical insight is lost among the algebra. In order to provide some physical insight into the solution, it is necessary to reduce the problem further. Thus, several more assumptions are made: (1)  $E_z \sim 0$ , i.e., only TE<sub>z</sub> modes are considered; (2)  $n = 0$ , axisymmetric modes; (3)  $n_e(r) = n_i(r) = \text{Constant}$ . Therefore the fields in the plasma are reduced to the following form:

$$E_r = \omega\mu_0\Lambda^{-1}k_0^2 D \frac{d}{dr} H_z \quad (13)$$

$$E_\phi = i\omega\mu_0\Lambda^{-1}(k_z^2 - k_0^2 S) \frac{d}{dr} H_z \quad (14)$$

$$H_r = ik_z\Lambda^{-1}(k_z^2 - k_0^2 S) \frac{d}{dr} H_z \quad (15)$$

$$H_\phi = k_z^2\Lambda^{-1}k_0^2 D \frac{d}{dr} H_z \quad (16)$$

where the variables  $\Lambda$ ,  $D$ , and  $S$  are defined in ref 6. The absorbed plasma power was shown to be

$$\mathcal{P}_1 = \frac{1}{2} k_0^2 \omega \mu_0 S_{IM} \frac{1}{|\Lambda|^2} \left| \frac{dH_z}{dr} \right|^2 \left\{ k_z^4 - 2k_z^2 k_0^2 S + \frac{k_0^4}{2} (R^2 + L^2) \right\} \quad (17)$$

$$\mathcal{P}_2 = \omega \mu_0 k_0^4 \left| \frac{dH_z}{dr} \right| \frac{1}{|\Lambda|^2} D_{Re} (k_z^2 - k_0^2 S_{Re}) D_{IM} \quad (18)$$



Examining the functional dependence of  $\mathcal{P}_1$  and  $\mathcal{P}_2$  yields

$$\mathcal{P}_1 \propto S_{im} \mathcal{L}_p \quad (19)$$

$$\mathcal{P}_2 \propto \frac{D_{Re} D_{Im}}{|\Lambda|^2} \quad (20)$$

where

$$\mathcal{L}_p = \frac{1}{\Lambda^2} \{k_z^4 - 2k_z^2 k_0^2 S + k_0^4 (R^2 + L^2)\} \quad (21)$$

$$\frac{(k_z^4 - 2k_z^2 k_0^2 S + k_0^4 (R^2 + L^2))}{(k_z^2 - k_0^2 R)^2 (k_z^2 - k_0^2 L)^2} \quad (22)$$

In the limit of  $\omega \rightarrow \omega_{ci}$  ( $L \rightarrow \infty$ ), it is seen that  $\mathcal{L}_p \rightarrow 1$ . Therefore

$$\lim_{\omega \rightarrow \omega_{ci}} \mathcal{P}_1 \propto \frac{\omega_{pi}^2}{\omega \nu_i} \mathcal{L}_p = \frac{\omega_{pi}^2}{\omega \nu_i} \quad (23)$$

$$\lim_{\omega \rightarrow \omega_{ci}} \mathcal{P}_2 \propto \frac{1}{|\Lambda|^2} \frac{\omega_{pi}^4 \omega_{ci}^2}{8 \omega^5 \nu_i} \quad (24)$$

The parametric dependences of the absorbed power can thus be seen and are shown in Table 1

Table 1: Parametric Dependence of the Absorbed Plasma Power

Plasma Property	Direction to maximize $P_{abs}$
Ion Temperature $T_i$	INCREASE
Plasma Density $n_e$	DECREASE
Plasma Radius $a$	INCREASE

## 2.2 Computational Analysis

Although the analytical treatment of the previous section yielded intuitive results of the dependence of  $P_{abs}$  on plasma parameters, it nevertheless is too simplified a treatment to apply to a real system. The main simplification that was made in the analytical treatment was the use of only one eigenmode. Although that allowed for a simple solution, the single

mode treatment is nevertheless too crude to be used. A typical solution that proved to be useful required the solution of about 30-50 modes which, upon summation, form the resulting field solutions.

Another limitation of the analytical approach is that it doesn't consider the issue of the field inhomogeneity. Again, this simplification was made in order to reduce the complexity of the problem. It is thus for these reasons that a computational analysis was deemed necessary and undertaken.

The goal of this computational analysis is to provide a better modeling of the wave-plasma coupling problem than the simplified results of the analytical solution. However, this computational analysis is not simply a purely numerical simulation. Much analytical work is done to reduce the fields to functional form, i.e.  $I_n(k_r r)$ ,  $K_n(k_r r)$ ,  $J_n(k_{\perp} r)$  before the numerical "number-crunching" is handed over to the codes.

The BEACH code extends the analytical approach taken in the cylindrical geometry solution of the previous section. It solves for the ICRF wave propagation in an inhomogeneous axial magnetic field. The inhomogeneous axial geometry is handled by separating the axial length into discrete axial "slices", each of which contains a homogeneous axial magnetic field.

The code first finds the eigenmodes that exist in each axial slice by satisfying both the infinite plasma dispersion relation and the boundary conditions. The boundary condition of the plasma-vacuum system can be written as:

$$c_1 H_p + c_2 E_p = c_1 J_\phi \quad (25)$$

$$c_3 H_p + c_4 E_p = c_2 J_\phi \quad (26)$$

The solution to the above are:

$$H_p = \frac{(c_1 c_4 - c_2 c_3)}{D} J_z \quad (27)$$

$$E_p = \frac{(c_2 c_1 - c_4 c_3)}{D} J_\phi \quad (28)$$

$$D = c_1 c_4 - c_2 c_3 \quad (29)$$

The term  $D$  is then the boundary condition of the bounded plasma-vacuum system. Solving this boundary condition coupled with the dispersion relation

$$SK_1^4 + k_1^2 [k_z^2 (S + P) - k_0^2 (SP + RL)] + P(k_z^2 - k_0^2 R)(k_z^2 - k_0^2 L) = 0 \quad (30)$$

yields the eigenmodes of the cylindrical system.

After solving for the eigenmodes of the system, the code then computes the excitation coefficients of the initial axial slice as driven by the source term (Antenna). The excitation coefficient of the next axial slice can then be determined by imposing two conditions of continuity on the boundary between the two axial slices: conservation of the integrated axially propagating Poynting Flux  $\int S_z^i r dr$ , and the continuity of wave phase. These two conditions uniquely determine the excitation coefficients of the different eigenmodes in the next axial slice. This analysis is then performed for all axial slices.

## 2.3 Computational Results

Computational analysis was performed on two types of plasma regimes: collisionless and collisional cold plasma. Different physics are inherent in each different regime.

### 2.3.1 Collisionless

Initially, the calculations of the ICRF field propagation were performed using a cold, collisionless plasma model. This ensures that there exist no complex  $k_z$  roots that could damp out the axially propagating Poynting Flux, thus enabling a good check of the model's ability to conserve power.

Several different antenna geometries are used to launch different modes. The two antenna geometries that were studied were the full turn loop and the half turn loop.

The baseline model is driven by a Full Turn Loop (FTL) antenna. Because it is symmetric in  $\theta$ , the full turn loop antenna excites only the  $n=0$  mode. Figures 1 and 2 show the propagation characteristic of the ICRF  $B_z$  and  $E_z$  fields as the waves propagate from the launch point ( $z=0$ ) towards the resonance point downstream. The results that are readily observable from this collisionless propagation of the  $n=0$  mode towards resonance are given below:

1.  $B_z$  Increases - This is an expected result. Stix shows (Stix, Theory of Plasma Waves, p.51, Eq(18) ) 8 that for a homogeneous lossless medium, the group velocity is

$$v_g = \frac{\mathcal{P} - T}{W_0} \quad (31)$$

$N=0$ ,  $N_E = 1.50 \times 10^{12}$ ,  $\omega/\omega_{ci0} = 0.788$ , COLD COLLISIONLESS MODEL  
NO. MODES = 30

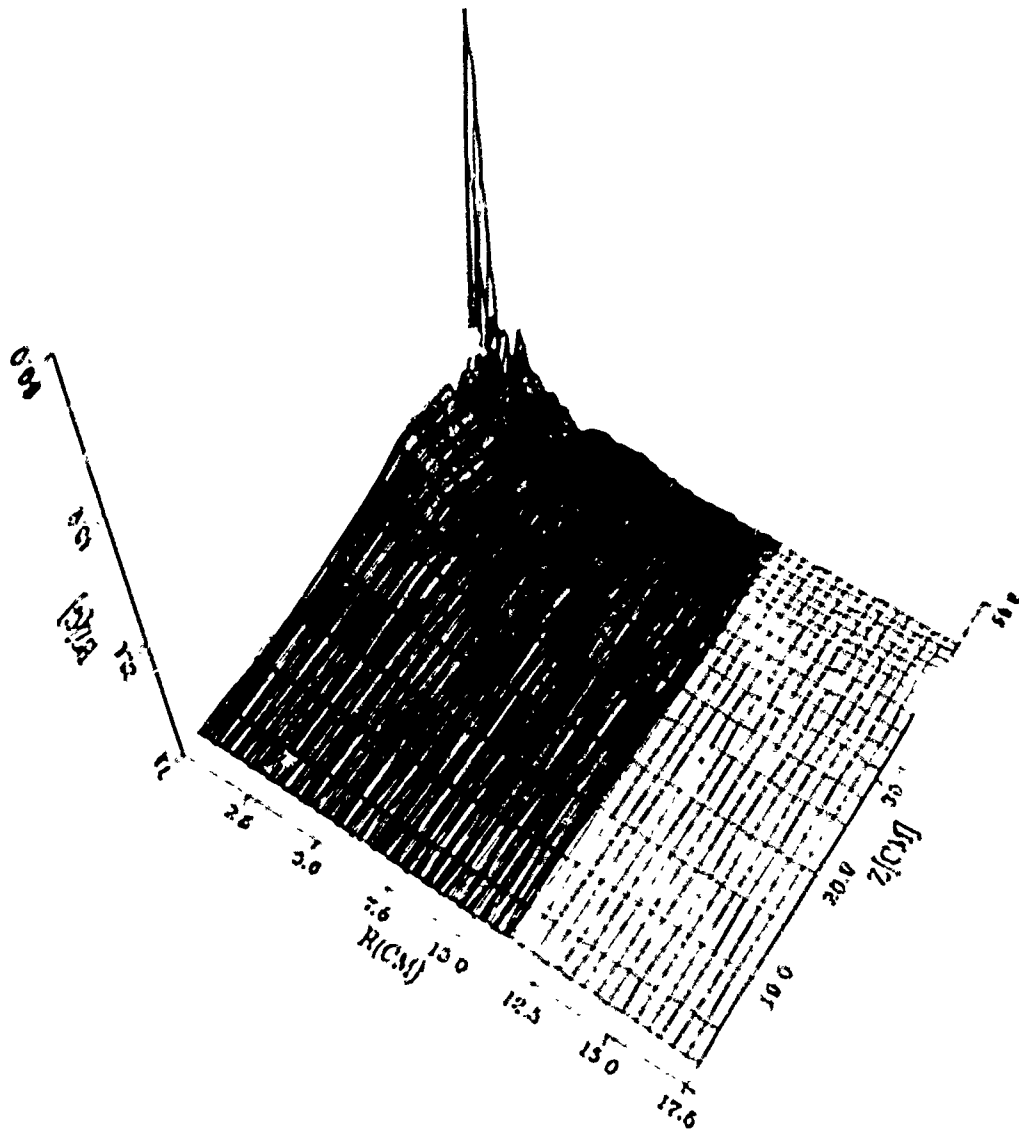


Figure 1: ICRF  $B_z$  Propagation in a Cold Collisionless Plasma, Full Turn Loop Antenna,  $\omega/\omega_{ci0} = 0.788$ . Waves are launched by the ICRF antenna at  $z = 0$  cm and propagate towards resonance at  $z = 50$  cm.

$N=0$ ,  $N_E = 1.50 \times 10^{12}$ ,  $\omega/\omega_{ci0} = 0.788$ , COLD COLLISIONLESS MODEL  
 NO. MODES = 30

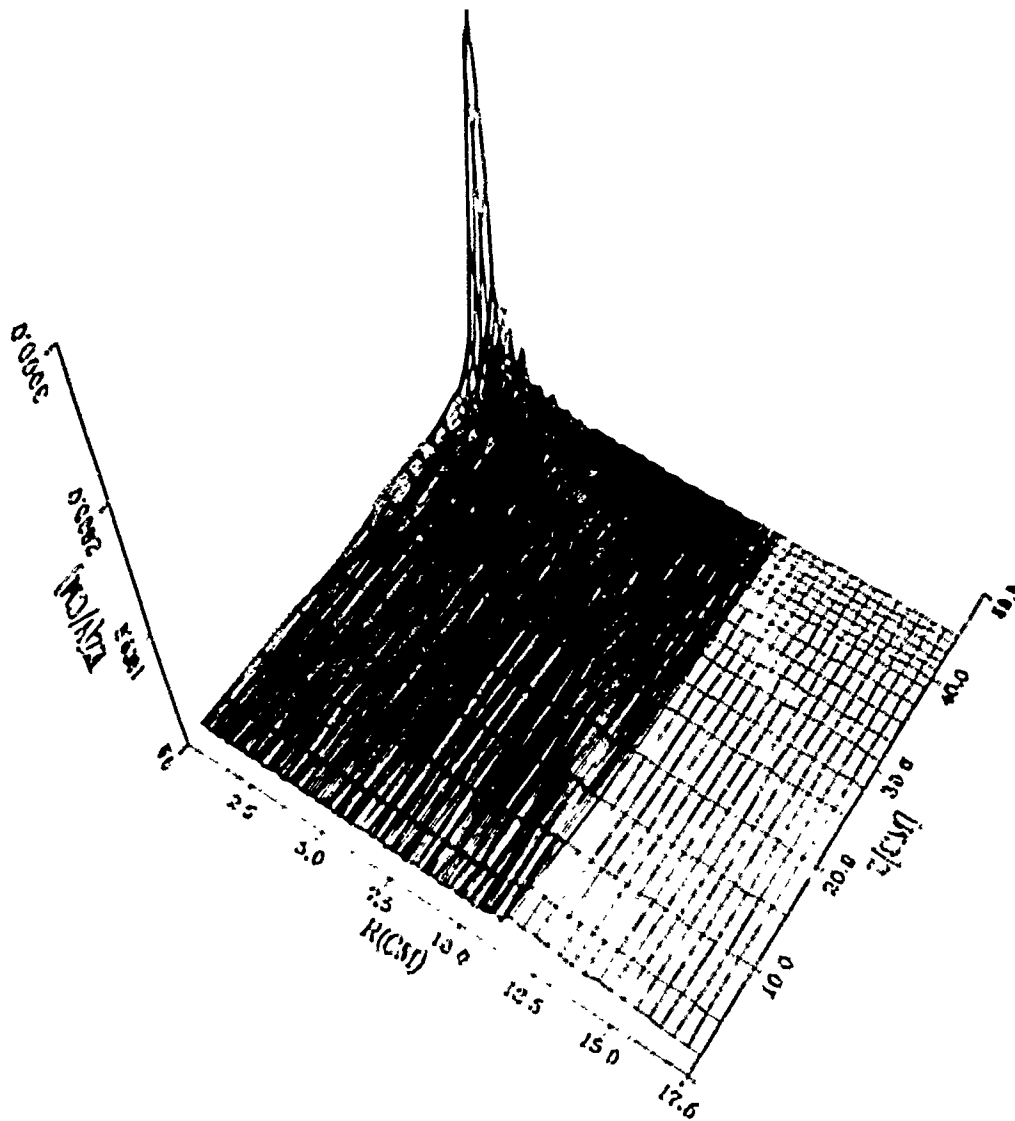


Figure 2: ICRF  $E_z$  Propagation in a Cold Collisionless Plasma, Full Turn Loop Antenna,  
 $\omega/\omega_{ci0} = 0.788$

When resonance is approached, the group velocity slows down, resulting in an increased energy density  $W_0$ . This increased energy density is apparent in the increase in  $|B_z|$ , since the energy density varies as

$$W_0 = \mu_0 \frac{B_z^2}{2} + \epsilon_0 \frac{E_z^2}{2} \quad (32)$$

2. Increase in axial and radial  $k_z$  - As resonance ( $\omega = \omega_{ce}$ ) is approached, the left hand cut-off ( $k_z^2 = k_0^2 L$ ) increases, causing an increase in the resulting  $k_z$  eigenmodes. This is consistent with the slowing down of the group and phase velocities as resonance is approached.
3. High edge electric fields  $E_r$ ,  $E_\theta$  and  $E_z$  that propagate inward - This is a result that could be consistent with experimental observation. Golovato points out (Personal communications) that although a high edge electric field is predicted by the ANTENNA code, experimentally no edge electric field is detectable. The BEACH simulation shows that the reason that no edge electric field is detectable is that the edge spike moves radially inward into the plasma as resonance is approached.
4. Higher order modes excited at higher amplitudes for lower initial  $\omega/\omega_{ce}$  - This result reflects the effect of the antenna excitation profile ( $J_0(k_z)$ ) on the excited EM field coefficients. For a lower  $\omega/\omega_{ce}$ , the value of the left-handed cut-off in the infinite plasma dispersion relation  $k_0^2 L$  decreases. Since the  $J_0(k_z)$  profile remains constant, this means that ALL modes are now excited to higher values. (See Figure ?? )

The solution of the dual half turn loop (DHTL) geometry poses a more difficult problem than the full turn loop (FTL) solution. The main difference between the DHTL and the FTL lies in the  $\tilde{J}(k_z)$  driving term, specifically the radial feeders. This is different from the Full Turn Loop (FTL) geometry in which the contribution from the radial feeders cancel out (Since one leg is entering and the other is exiting, net  $J_r$  is zero). The modelling of the driving term  $\tilde{J}(k_z)$  for the DHTL is detailed in a full report in preparation.

The basic characteristics of ICRF propagation towards resonance are similar to the FTL ( $n=0$ ) case, i.e. increasing  $k_z$  and  $k_\perp$ , and increasing  $B_z$  amplitude. The main difference is the larger  $k_\perp$  and  $k_z$  for the DHTL case, which is to be expected since the asymmetric

(about  $\tau = 0$ ) DHTL excitation necessitates radial eigenmodes that have smaller perpendicular wavelengths (larger  $k_\perp$ ) and hence larger  $k_z$ .

The  $E_z$  field also appears to be similar in structure to the FTL case, with an initial edge peaked  $E_z$  that propagates towards the center of the plasma as resonance is approached.

### 2.3.2 Collisional

The presence of collisions, of course, implies a finite temperature. The *Cold Plasma Collisional Model* means that the expansion of the plasma  $Z$ -function excludes temperature effects and keeps only terms of  $O(\nu_i, \omega)$ . The code results for the case of ICRF propagation in a cold collisional plasma is seen below in Figure 3.

The presence of collisions manifests itself in a complex dielectric tensor. Recall that the dielectric tensor is given by

$$\epsilon = \begin{bmatrix} S & iD & 0 \\ iD & S & 0 \\ 0 & 0 & P \end{bmatrix} \quad (33)$$

where

$$S = \frac{1}{2}(R + L) \quad (34)$$

$$D = \frac{1}{2}(R - L) \quad (35)$$

The presence of collisions in a cold plasma produces the following expansions for  $S$ ,  $D$ , and  $P$

$$S = 1 - \sum_n \frac{\omega_{pn}^2}{\omega} \left\{ \begin{array}{l} \omega(\omega^2 - \omega_n^2 + \nu_i^2) \\ i\nu_i(\omega^2 + \omega_{cn}^2 + \nu_i^2) \end{array} \right\} \quad (36)$$

$$D = \frac{\omega_p^2 \omega_{ci}}{\omega} \frac{(\omega^2 - \omega_{ci}^2 - \nu_i^2 - 2i\omega\nu_i)}{(\omega^2 - \omega_{ci}^2 - \nu_i^2)^2 + 4\omega^2\nu_i^2} \quad (37)$$

$$P = 1 - \sum_n \frac{\omega_{pn}^2}{\omega(\omega^2 - \omega_{cn}^2)} \quad (38)$$

Using these complex elements of the dielectric tensor, the dispersion relation can be solved with the geometric boundary condition to yield a set of eigenmode solutions for this plasma vacuum geometry. The difference between these solutions and those of the cold collisionless

$N=0$ ,  $N_E=1.00 \times 10^{18}$ ,  $W/W_{C10}=0.788$ , COLD COLLISIONAL MODEL  
 $T_I\text{-PERP}=10.00$ ,  $T_E\text{-PERP}=10.00$ ,  $T_I\text{-Z}=10.00$ ,  $T_E\text{-Z}=10.00$   
 NO. MODES = 30

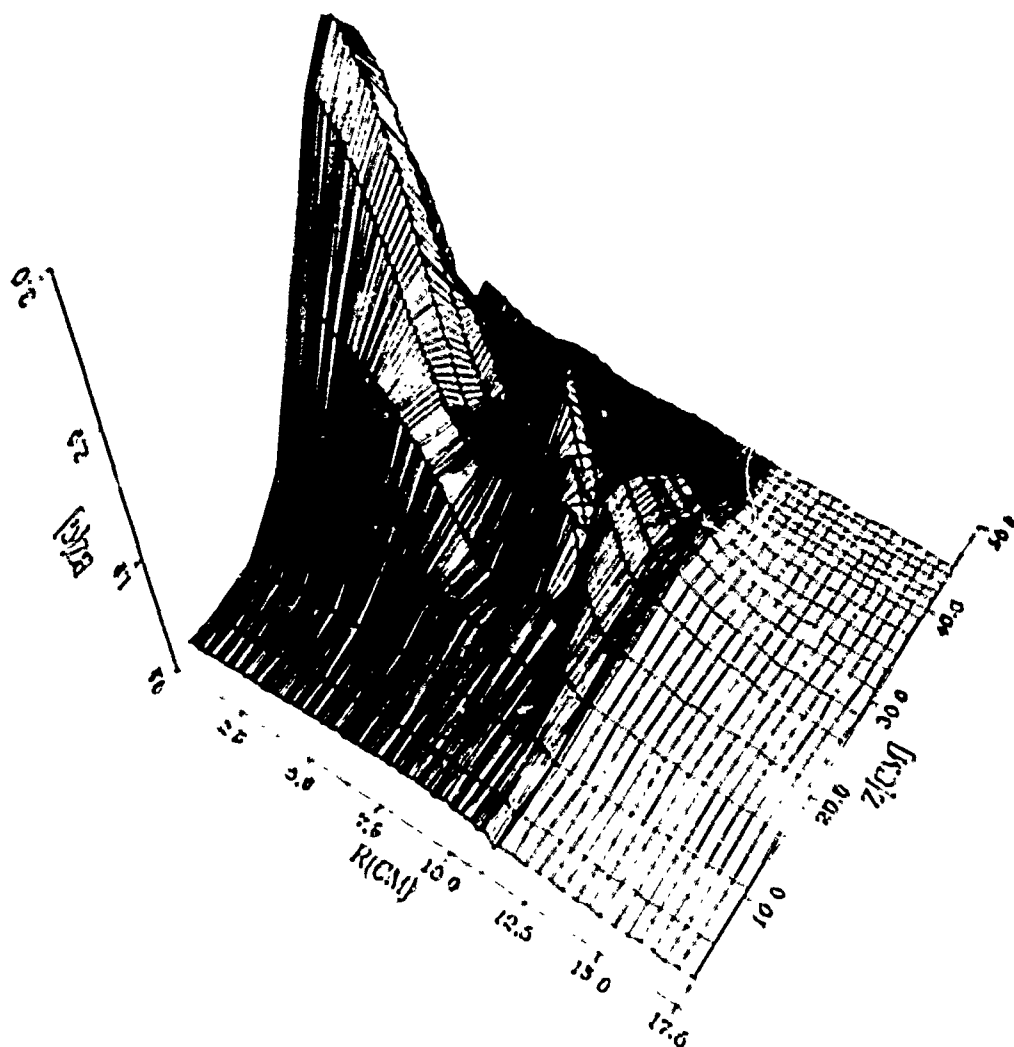


Figure 3: ICRF  $B_z$  Propagation in a Cold Collisional Plasma, Full Turn Loop Antenna,  
 $\omega/\omega_{C10}=0.788$



$N=0$ ,  $N_E = 1.00 \times 10^{18}$ ,  $W/W_{C10} = 0.788$ , COLD COLLISIONAL MODEL  
 $T_I\text{-PERP} = 10.00$ ,  $T_E\text{-PERP} = 10.00$ ,  $T_I\text{-Z} = 10.00$ ,  $T_E\text{-Z} = 10.00$   
 NO. MODES = 30

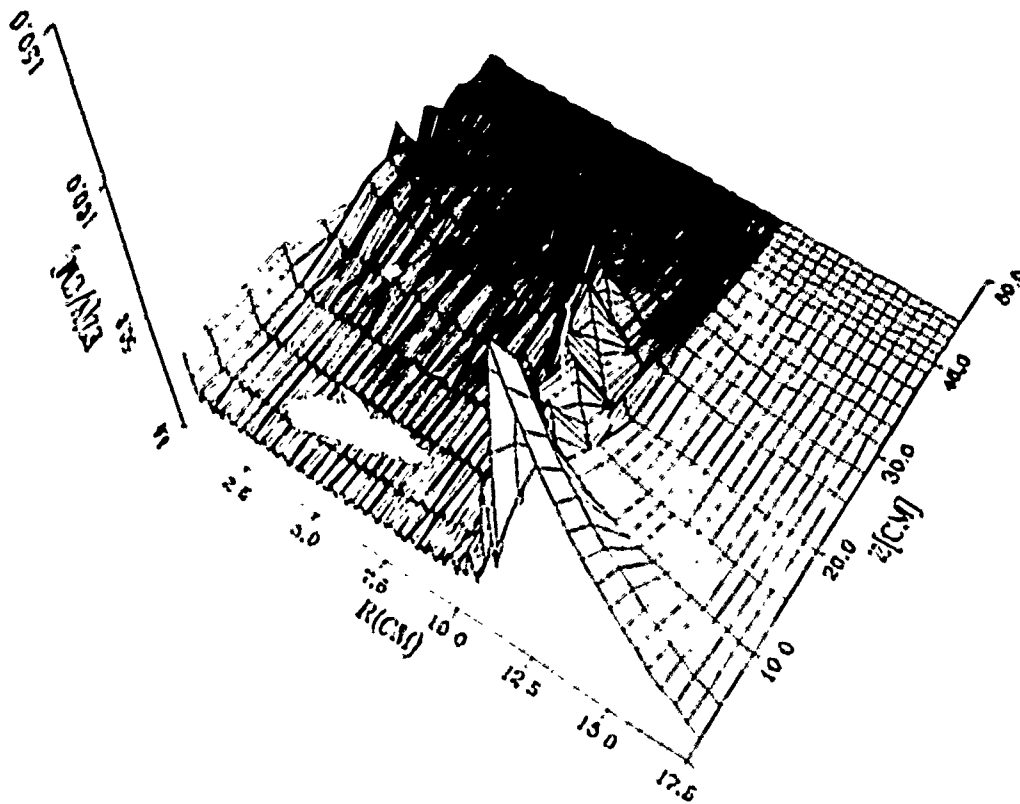


Figure 4: ICRF  $E_z$  Propagation in a Cold Collisional Plasma, Full Turn Loop Antenna,  
 $\omega/\omega_{cu} = 0.788$

plasma is that the  $k_z$  eigenmodes are now complex - these waves are now damped as they propagate towards the cyclotron resonance. This damping transfers energy from the waves to the plasma, causing plasma heating.

### 3 Progress In Experimental Program

#### 3.1 Diagnostics

In order to determine the plasma characteristics of the discharge produced, an adequate set of diagnostics must be assembled to measure some basic plasma parameters. These parameters include the ion temperature  $T_i$ , electron temperature  $T_e$ , and electron and ion densities  $n_e$ ,  $n_i$ . A system of diagnostics was designed, fabricated or reconstructed, calibrated and used to determine plasma properties as part of this experiment. This section will discuss the diagnostics systems that were fabricated and/or reconstructed for use on this experiment.

The diagnostics currently operating are listed in Table 2 along with the plasma properties that they measure. The principle of these diagnostics and their operation and method of analysis are evaluated and presented below.

Table 2: PPEX Diagnostic Set

DIAGNOSTIC	LOCATION	PLASMA PROPERTY MEASURED
LANGMUIR PROBE	CC	$T_e(a), n_e(a)$
INTERFEROMETER	CC, Anchor	$n_e$
$H_\alpha$ ARRAY	CC, Anchor	$n(r)$
SPECTROMETER	Anchor	$T_i, n_i$ , Plasma Rotation
DIAMAGNETIC LOOP	CC	$\beta, n_e, T_i + T_e$
B-DOT PROBE	CC	$k_z$ , ICRF Propagation

### 3.1.1 Langmuir Probe

The basic principle of the Langmuir is well-known and is briefly described to the method of analysis used here. A Current-Voltage characteristic curve is produced when the probe driving voltage is swept from some negative value to a positive value (H& L, p.115)ref[9]. At negative voltages, the probe should attract only ions at an ion saturation flux found to be (Huddleston, Leonard, p.150) ref[9]

$$I_{sat} = \frac{1}{2} n_0 A \left( \frac{kT_e}{M} \right)^{\frac{1}{2}} \quad (39)$$

where  $A$  is the probe area,  $n_0$  the plasma density, and  $M$  the ion mass. As the probe voltage is increased, more and more electrons can penetrate the negative potential until a floating potential  $V_f$  is eventually reached. The probe being at the floating potential means that the net inward electron flux equals the net inward ion flux. As the voltage is continuously raised, the probe now attains a linear regime in which the electron current behaves in an exponential manner, assuming a Maxwellian electron distribution (H& L, p.135). This is known as the transition region and has the characteristic:

$$I = A_p n_0 \left( \frac{kT}{2\pi m} \right)^{\frac{1}{2}} e^{eV/kT}$$

From experimental observations of the current-voltage characteristic, the electron temperature  $T_e$  and density  $n_e$  can be found. To calculate the electron temperature, the slope of the transition region is used. Taking the region of constant slope in this region, the electron temperature can be found from (Hutchinson, p.64) ref[10]

$$T_e = \frac{e(I - I_{sat})}{dI/dV} \quad (40)$$

where  $I$  is the Langmuir probe current in the middle of the linear region,  $\frac{dI}{dV}$  is the slope of the Langmuir Probe  $I-V$  characteristic of the linear region, and  $I_{sat}$  the ion saturation current.

From this value of the electron temperature, the edge plasma density can be found from the ion saturation current  $I_{sat}$  (Hutchinson, p.60):

$$I_{sat} = n_{\infty} A_s C_s q e^{-\frac{1}{2}}$$

where  $A_p$  is the area of the Langmuir Probe tip,  $C_s$  the ion sound speed ( $C_s = (T_e/m_i)^{1/2}$ ). The density is then found to be

$$n_{ee} = \frac{I_{ap} e^{1/2}}{A_p C_s q} \quad (41)$$

### 3.1.2 Interferometer

The basic principle of plasma interferometry utilizes the phase shifting of the plasma O-mode wave whose dispersion relation is

$$\omega^2 = \omega_{pe}^2 + c^2 k^2$$

where

$$\omega_{pe}^2 = \frac{e^2 n_{ee}}{\epsilon_0 m_e}$$

is the electron plasma frequency. The index of refraction can then be defined as :

$$N = \frac{ck}{\omega} = \left[ 1 - \frac{\omega_{pe}^2}{\omega^2} \right]^{1/2}$$

The phase change due to the wave propagating in the plasma medium of length  $l$  (in addition to its normal propagation in vacuum) is then

$$\Delta\phi = kl(N - 1)$$

From the measured value of the  $\Delta\phi$ , the line averaged electron density can be found by:

$$n_e = \frac{\omega^2 \epsilon_0 m_e}{e^2} \left( 1 - \left[ 1 - \frac{\Delta\phi}{kl} \right]^2 \right) \quad (42)$$

### 3.1.3 Frequency Sweeping Operation

The above is for a homodyne interferometer. The interferometer used in the PPEX experiment is a frequency-swept interferometer. The basic principle of the phase shift is the same as that of the homodyne interferometer, the difference being that the frequency of the interferometer is swept over a fixed range. Sweeping frequencies from 100KHz to 1MHz have been used. The interferometer in the PPEX experiment utilizes a 80KHz ramp generator to produce the sweeping frequency.

For such a frequency swept interferometer, the phase shift is given by

$$\Delta\phi = 2\pi \times 1.34 \times 10^{-16} \frac{1}{f_0(\text{GHz})} \int n_e(x,t) dx (m^{-2})$$

For the 35GHz interferometer used on the PPEX, this works out to be

$$\Delta\phi = 4.81 \times 10^{-16} n_e \Delta x$$

or, using an average plasma radius of 10cm,

$$n_e = \Delta\phi \times (2.08 \times 10^{11} cm^{-3}) \quad (43)$$

where  $\Delta\phi$  is the phase shift in radians.

### 3.1.4 Spectrometer

The Doppler shift due to a source moving parallel (with velocity  $v_s$ ) to the direction of observation is

$$\Delta\lambda = \pm \frac{v_s}{c} \lambda$$

It can be shown (H&L, p.268)ref 9 that for sources of Maxwellian velocity distribution,

$$I(\Delta\lambda) = \frac{I_t}{\pi^{1/2} \Delta\lambda_D} \exp \left[ - \left( \frac{\Delta\lambda}{\Delta\lambda_D} \right)^2 \right]$$

where  $I_t$  is the total line intensity. The intensity is half its maximum value when the exponential reaches  $\frac{1}{2}$ . The full width half max (FWHM) (H&L, p.269) line width is found to be

$$\Delta\lambda_{1/2} = 7.16 \times 10^{-7} \lambda (T/M)^{1/2}$$

( $T_i$  is in degrees Kelvin,  $M$  is the molecular wt of the ion) Therefore the ion temperature is found to be

$$T_i = \frac{\Delta\lambda_{1/2}^2}{(7.16 \times 10^{-7} \lambda)^2} \quad (44)$$

The rotating mirror assembly is constructed to convert the J-A Monochromator Spectrometer into a scanning spectrometer. The reason for using a rotating mirror assembly is to translate the incoming beam by a glass slide, hence shifting the wavelength entering the photomultiplier slit.

Using Snell's Law, the amount of beam translation is found to be

$$\delta x = t \sin \theta_i \left( 1 - \frac{\cos \theta_i}{\sqrt{n^2 - (\sin \theta_i)^2}} \right)$$

By translating the beam with a rotating glass slide, the wavelength that is being examined by the photomultiplier assembly is thus caused to vary.

### 3.1.5 $H_\alpha$ Array

The basic  $H_\alpha$  array constructed for use on the PPEX is a multi-chord photomultiplier system. The basic principle of the Multichord Array is that of a pinhole camera. Light from the plasma passes through a pinhole and is subsequently detected by the photodetector array on the end of the array holder. Arbitrary filters may be installed over the pinhole to allow viewing of different light, be it impurity or plasma emissions.

### 3.1.6 Diamagnetic Loop

The diamagnetic loop is a magnetic field probe that is positioned around the plasma. The loop detects the magnetic flux that it surrounds and the voltage induced on the loop is subsequently measured and processed to yield the plasma beta.

Using Maxwell's equations and the MHD Equilibrium condition, it can be shown that the magnetic field inside a plasma of finite  $\beta$  is given by

$$B_z = \sqrt{1 - \beta} B_0$$

where  $\beta$  is defined as the ratio of the plasma pressure to the magnetic field pressure,  $\beta = P / (B^2 / 2\mu_0)$ . The flux that passes through the diamagnetic loop is then found to be

$$\Phi_{z, \text{total}} = N \left( \int_0^{r_p} B_z 2\pi r dr + \int_{r_p}^{r_1} B_0 2\pi r dr \right)$$

The plasma contribution is then seen to be

$$\Phi_{z, P} = \frac{N \beta B_0^2 \pi r_p^2}{2}$$

The output voltage that is induced in the loop is RC integrated to yield the magnetic flux and is seen to be

$$V_0 = \frac{\Phi_{z, P}}{RC}$$

Thus the plasma  $\beta$  can be found directly from this output voltage and is seen to be

$$\beta = \frac{2RC}{N^2 B_0^2 \pi r_p^2} \gamma V_0$$

where the factor  $\gamma$  takes into account the frequency response of the diamagnetic loop.

### 3.1.7 B-Dot Probe

The B-Dot probe picks up the ICRF fluctuating magnetic fields that are either propagating in the plasma or evanescent but still detectable. The B-Dot Probe works with a similar principle to the Diamagnetic Loop, namely that the time-varying RF field is picked up and read as an induced loop voltage  $V$ , where

$$V = \frac{d}{dt} \int \vec{B} \cdot d\vec{A}$$

This induced loop voltage can then be detected and digitized.

## 3.2 ICRH Wave Experimental

### 3.2.1 experiment set-up

The schematic of the experiment is shown in Fig. 5. There are double half-loop antennae in the south end cell and in the north end of the central cell. Both antennae are located at fields higher than the corresponding ones for their resonant frequencies ( $\omega < \omega_n$ ). The frequency of the rf power is in resonance with the ion cyclotron frequency at the field of the midplane of each cell. When rf radiation was emitted at the antennae, the wave excited in the plasma travels both radially inward and axially toward the center of each cell. The diagnostics enclosed by the box in Fig. 5 are currently operational which were built and installed in the past year. A scanning spectrometer and a retarding field grid energy analyzer will be installed later.

### 3.2.2 experimental results

The B-dot probe allows the measurement of  $\vec{B}_r$ ,  $\vec{B}_\theta$  and  $\vec{B}_z$ .  $\vec{B}_r$  and  $\vec{B}_\theta$  were very small. The Fourier spectrum of  $\vec{B}_z$  is shown in Fig. 6 is the wave in the vacuum. The fundamental

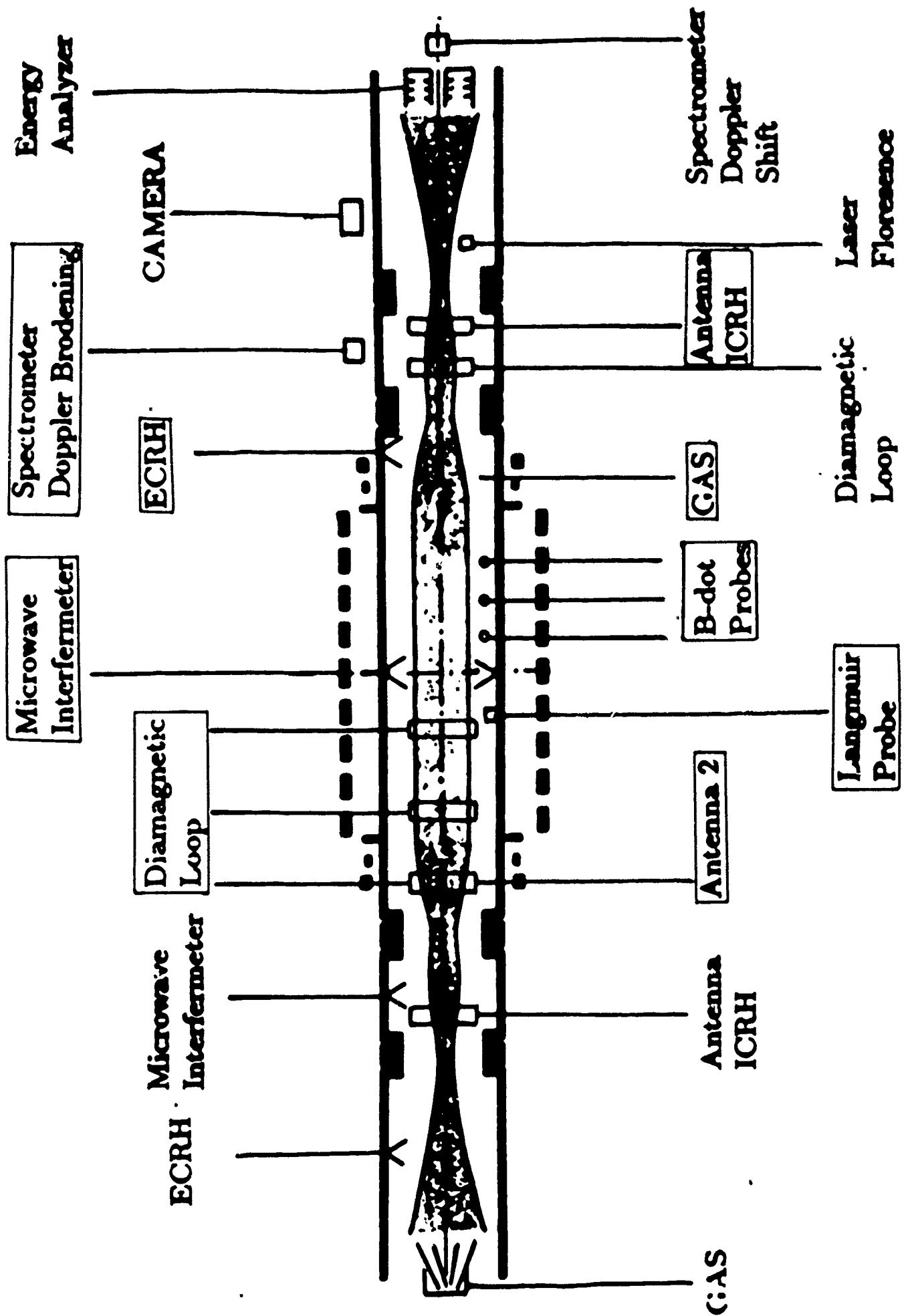


Figure 5: Diagnostic layout



frequency is 3 MHz marked by 0. The harmonics are marked by 1,2,3 and 4. The peaks in between may be due to the imperfection of the rf transmitter. A comparison of Figs. 6a and 6b shows that the amplitude of fundamental frequency peak 0 is one unit in the vacuum and 50 units in the plasma. The half-width is about 0.1 MHz for the vacuum and 1 MHz for the plasma. Therefore the amplitude of the wave is 50 times higher in the plasma than in the vacuum at the resonance which confirms the theoretical prediction. The width of the wave is 10 times broader. The reason that the plasma signals are much larger than the vacuum signals is that the ICRF  $\bar{B}_2$  is evanescent in the vacuum, while the presence of the plasma allows it to propagate. This large broadening indicates increasing resistance due to the loading of plasma. There is little evidence that the wave injected in the end cell will propagate into the central cell or vice versa because of the fact that the wave energy is damped and absorbed near the resonance in the respective cells. There is also little evidence of heating electrons at the edge, an indication of less loss and higher efficiency.

### 3.2.3 Plasma Broadening of ICRF Spectrum

One of the discoveries made on this plasma propulsion experiment is the broadening of the ICRF Fourier spectrum in the presence of a plasma. Comparison of a vacuum ICRF shot to a plasma ICRF shot clearly shows this effect. We propose an explanation for this effect. The broadening is thought to be caused by the detuning of the plasma  $Q$  as defined by

$$Q = \frac{\int \omega L}{\Delta f R}$$

Since the antenna was originally tuned for vacuum, the  $Q$  is very large for a vacuum shot (hence a narrow peak). However, the presence of a plasma increases the serial resistance of the equivalent RLC resonance circuit, therefore  $Q = \frac{\omega L}{R}$  decreases, causing  $\Delta f(\propto \frac{1}{Q})$  to increase.

### 3.2.4 Instability

To understand the resonance effect two types of experiments were carried out: To inject the rf power at a frequency slightly higher or lower than the resonance frequency. Therefore we called the class of discharges with  $\omega > \omega_c$  as type I and the class of discharges with

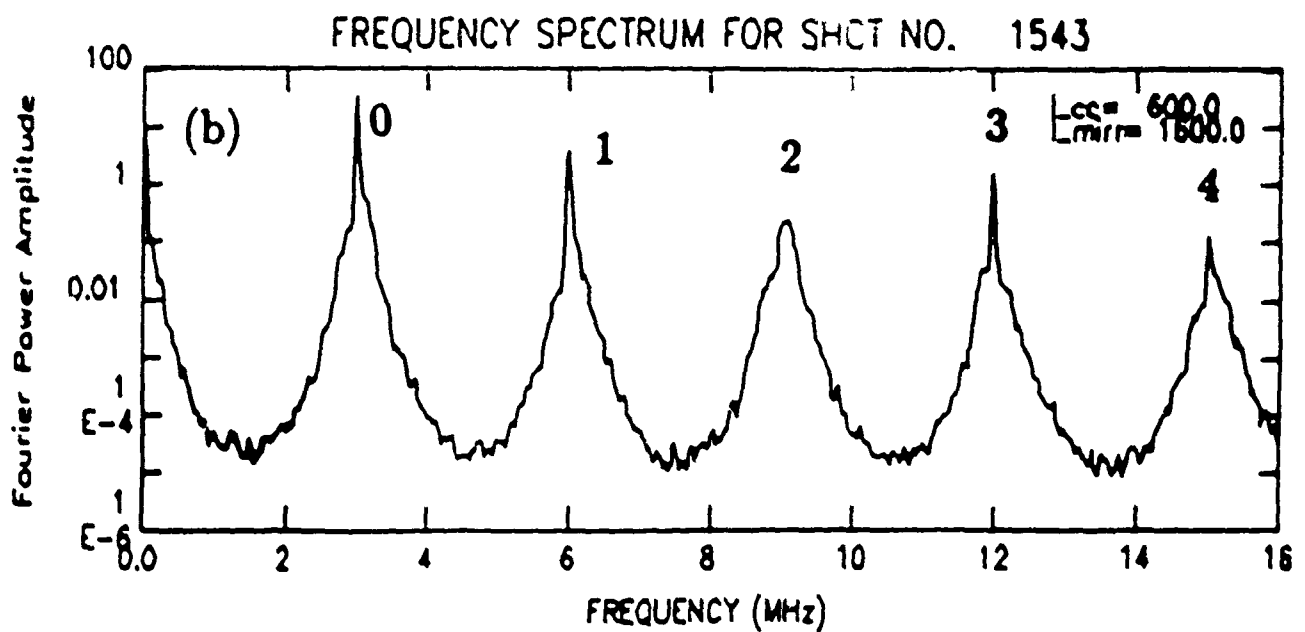
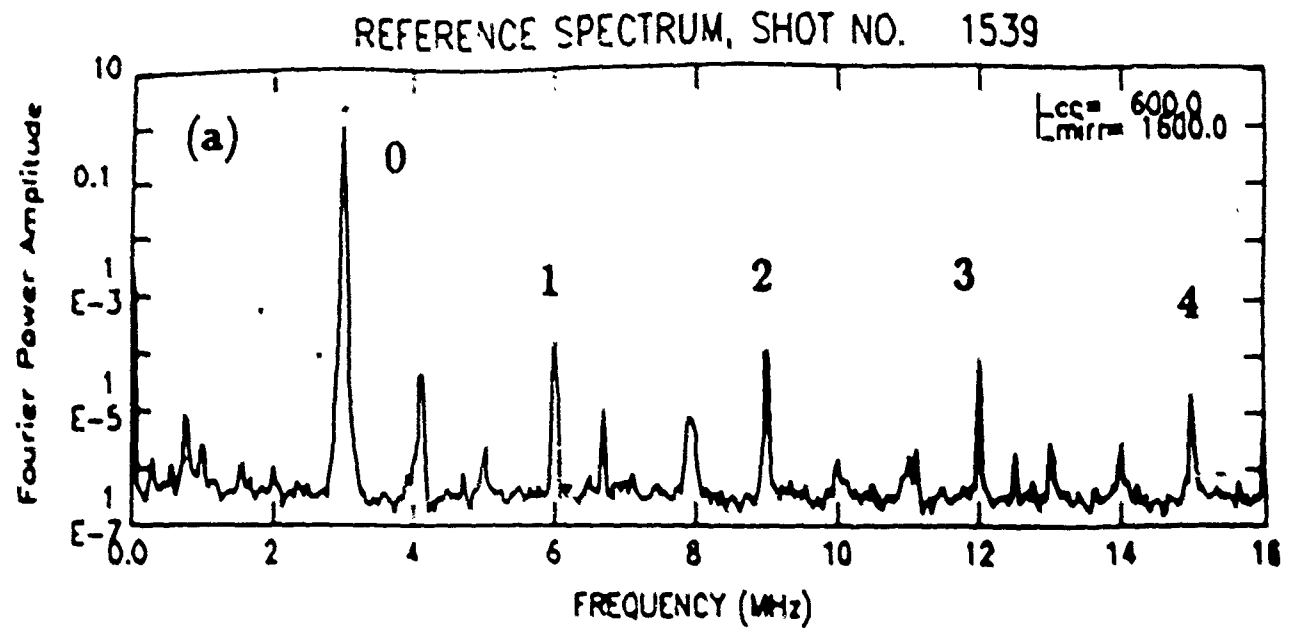


Figure 9: Fourier spectrum of the measured wave of frequency of  $3MHz$ : (a) in the vacuum and (b) in the plasma. The amplitude and width of the wave in the plasma are much larger than in the vacuum.

$\omega \sim \omega_{UH}$  as type II. Figure 7 shows the H- $\alpha$  acquired during TYPE I and II discharges. There are distinguish features between these two types of H- $\alpha$  emissions. For the first type, There is strong fluctuations initially which decays and becomes quiescent. This indicates the instability at the initial phase of the discharge. Fortunately it was stabilized possibly due to the ponderomotive force of the rf wave. The plasma is quiescent for the type II discharge although the amplitude of the H- $\alpha$  emission is modulated. This modulation may be due to the ECRH pulse or plasma rotation which has to be carefully investigated..

To find out the physical nature of the instability and its stabilizing mechanism for the type I discharge and source of the modulation for the type II discharge will be the center of our research effort. To do so additional diagnostics are needed, such as B-dot probe array, Langmuir probe array, retarding field grid energy analyzer and charge exchange analyzer.

In addition to the results presented above large amount of data have been collected. Detailed analysis is underway.

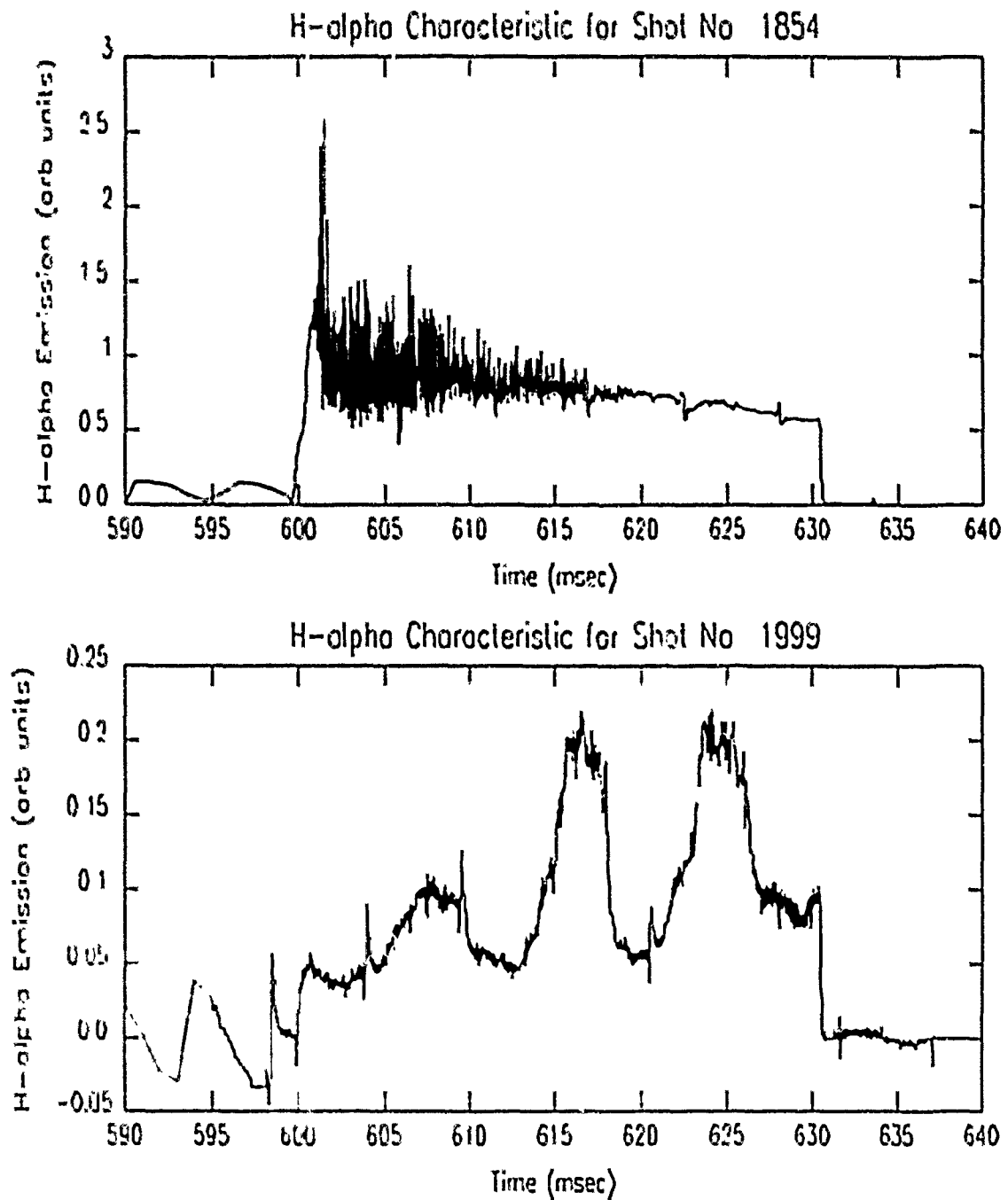


Figure 7: Comparison between the H- $\alpha$  output of TYPE I and TYPE II discharges. TYPE I (Top) shows a much higher light emission level as well as the three different regions identified as Ramp-up, Oscillatory, and Quiescence. TYPE II (Bottom) shows little light emission and is relatively quiescent.

## References

1. F.R. Chang and J.L. Fisher. *Nuclear Fusion*, 22(8), 1970.
2. F.R. Chang, W.A. Krueger, and T.F. Yang. In *AA/DBLR/JSASS Int. Electric Propulsion Conference*, paper AA-85-2049, Alexandria, 1985.
3. T.F. Yang, R.H. Miller, K.W. Wenzel, and W.A. Krueger. In *AA/DBLR/JSASS Int. Electric Propulsion Conference*, paper AA-85-2049, Alexandria, 1985.
4. F.R. Chang-Diaz, T.F. Yang, W.A. Krueger, S. Peng, J. Urbahn, X. Yao, and D. Griffin. In *DGLR/AA/JSASS Int. Electric Propulsion Conference*, paper DGLRA-88-126, Garmisch-Partenkirchen, W. Germany, 1988.
5. T.F. Yang, F.R. Chang-Diaz, S. Peng, J. Urbahn, and X. Yao. In *AA/ASME/SAE/ASEE, 25th Joint Propulsion Conf.*, paper AA-89-2383, Monterey, CA, 1989.
6. Scott Peng. Wave propagation in tandem mirror plasma propulsion device. Technical Report To be Published, Plasma Fusion Center, 1990.
7. B.D. McVey. Excitation theory of the inductive drive. Technical Report TASK II-2740, TRW, 1984.
8. T.H. Stix. *The Theory of Plasma Waves*. McGraw-Hill, 1962.
9. R.H. Huddleston and S.L. Leonard. *Plasma Diagnostic Techniques*. Academic Press, 1965.
10. I.H. Hutchinson. *Principles of Plasma Diagnostics*. Cambridge University Press, 1987.